ADVANCED MATERIALS
www.advmat.de

Carbonization-Temperature-Dependent Electrical Properties of Carbon Nanofibers—From Nanoscale to Macroscale

*Julian Borowec, Victor Selmert, Ansgar Kretzschmar, Kai Fries, Roland Schierholz, Hans Kungl, Rüdiger-A. Eichel, Hermann Tempel, and Florian Hausen**

An exact understanding of the conductivity of individual fibers and their networks is crucial to tailor the overall macroscopic properties of polyacrylonitrile (PAN)-based carbon nanofibers (CNFs). Therefore, microelectrical properties of CNF networks and nanoelectrical properties of individual CNFs, carbonized at temperatures from 600 to 1000 °C, are studied by means of conductive atomic force microscopy (C-AFM). At the microscale, the CNF networks show good electrical interconnections enabling a homogeneously distributed current flow. The network's homogeneity is underlined by the strong correlation of macroscopic conductivities, determined by the four-point-method, and microscopic results. Both, microscopic and macroscopic electrical properties, solely depend on the carbonization temperature and the exact resulting fiber structure. Strikingly, nanoscale high-resolution current maps of individual CNFs reveal a large highly resistive surface fraction, representing a clear limitation. Highly resistive surface domains are either attributed to disordered highly resistive carbon structures at the surface or the absence of electron percolation paths in the bulk volume. With increased carbonization temperature, the conductive surface domains grow in size resulting in a higher conductivity. This work contributes to existing microstructural models of CNFs by extending them by electrical properties, especially electron percolation paths.

1. Introduction

Electrospun polyacrylonitrile (PAN) based carbon nanofibers (CNFs) are promising next generation candidates for applications as electrodes in sensors,[1–4] electrical devices,[5] electrochemical catalysis,[6] and energy conversion and storage,[7–9] based on their high surface area and conductive properties. Additional superior adsorption properties,[10,11] such as high CO_2 selectivities, enable the utilization of CNFs as carbon capture material.[12–15] Furthermore, the interplay of both, electrical and adsorption properties, is essential for electrical conductive adsorbents employed in the energy efficient electrical swing adsorption (ESA) process.[16–18] To tailor the overall macroscopic properties of the CNFs to the respective application, an exact understanding of the micro- and nanoscale electrical properties of individual fibers and of the fiber networks is crucial.

Over the last decades, many studies analyzed the CNFs with a broad variety of analytical techniques, including scanning electron microscopy (SEM), transmission electron microscopy (TEM), X-ray diffraction (XRD), and Raman spectroscopy to characterize the CNFs' morphology, structure and their physical and chemical properties.[7,12,19–27] A strong influence of the exact preparation conditions, typically stabilization and subsequent carbonization, are found. The as-spun fibers are stabilized in air at temperatures between 200 and 300 °C.[12,25,28] Thereby, cyclization of nitrile and incorporation of oxygen takes place and the conjugated structure forms.[29] Subsequently, throughout the carbonization step at elevated temperatures under inert gas atmosphere the

J. Borowec, V. Selmert, A. Kretzschmar, K. Fries, R. Schierholz, H. Kungl, R.-A. Eichel, H. Tempel, F. Hausen
Institute of Energy and Climate Research – Fundamental Electrochemistry (IEK-9)
Forschungszentrum Jülich GmbH
52425 Jülich, Germany
E-mail: f.hausen@fz-juelich.de

J. Borowec, V. Selmert, R.-A. Eichel, F. Hausen
Institute of Physical Chemistry
RWTH Aachen University
52074 Aachen, Germany

The ORCID identification number(s) for the author(s) of this article can be found under https://doi.org/10.1002/adma.202300936

DOI: 10.1002/adma.202300936

crosslinking of the cyclisized polymer structure through denitrogenation occurs, resulting in a partially crystalline graphitic structure, whereby the fiber network becomes conductive.[29] Scanning tunneling microscopy (STM) revealed that the CNF's surface consists of both graphitic crystalline domains but also disordered domains.[30] It has been observed that with increasing the carbonization temperature the crystallite sites grow.[19,21–23,25] Accordingly, the amount of sp^2-hybridized (i.e., graphitic) carbon increased with carbonization temperature,[7] resulting in an increased order of carbon structures,[31] and thus, overall conductivity. The order of carbon structure was also enhanced by templating with nanoparticles,[32,33] and hot-drawing treatment of as-spun CNF mats.[33–35] Furthermore, higher carbonization temperatures may result in improved contacts of interconnected CNFs within the network,[20] thus promoting a high macroscopic conductivity.[25]

While there are many studies dealing with macroscopic conductivity measurements,[7,19–21,26,27,33,36,37] reports investigating the intrinsic electrical properties of carbon nanomaterials are scarce. One possibility to analyze microscopic electrical properties is the microscopic four-point-method,[38,39] which was carried out on multiwalled carbon nanotubes (MWNT) to investigate their electrical breakdown.[40] Another possibility are two-electrode-setups, created by spinning single PAN CNFs between two contacts.[41,42] Thereby, the conductivity of a single CNF carbonized at 800 °C was reported to be 4.9 S cm^{-1}[42], while a CNF carbonized at 900 °C exhibited a conductivity of 130 S cm^{-1}.[41] As an alternative two-electrode-setup, conductive atomic force microscopy (C-AFM) enables a simultaneous structural and electrical analysis, whereby defects in the structure of individual carbon nano tubes (CNTs) were found to cause a substantial increase in the intrinsic resistivity.[43] The spatial resolution allows C-AFM techniques the direct imaging of local electron percolation paths.[44] So far, C-AFM has been used on CNFs to analyze the effect of additives on the local conductivity. Ag nanoparticles have been found to improve the nanoelectrical properties,[45] and iron oxide nanoparticles have been found to increase the local measured currents and lead to composite CNFs with a higher specific capacity than the pure CNFs.[46]

This study reveals the effect of the carbonization temperature on nano- and microscale electrical properties of CNFs and their networks. Therefore, as in previous works,[7,12–15,22,23] different electrospun PAN-based CNF mats carbonized at temperatures within the range of 600–1000 °C were prepared, and each sample has been investigated by PeakForce Tunneling Atomic Force Microscopy (PF TUNA, Bruker), a force–distance curve based C-AFM mode. First, at the microscale, the interconnections of multiple fibers were investigated for each sample. Second, high resolution 200 nm × 200 nm maps of single CNFs within the networks of each sample were analyzed regarding their nanoscale conductive surface domains. Furthermore, the microscopically measured currents of each sample were quantified and correlated with macroscopic conductivities.

2. Results and Discussion

2.1. SEM Analysis

The microscale fibrous morphology of CNFs, carbonized at 600, 800, and 1000 °C is demonstrated by SEM images shown in **Figure 1**a–c, respectively. All CNF mats exhibit overlapping and randomly oriented fibers. Most CNFs are straight, a few exhibit curves and very few are broken, such as seen in Figure 1a. The detailed diameter analysis of two SEM images acquired on different spots for each sample (Figure 1a–c; Figure S1a– c, Supporting Information), by means of the DiameterJ algorithm,[47] is shown in Figure 1d–f. The average diameters of the CNFs, shown in Figure 1a–c, were found to be 279 ± 45, 252 ± 23, and 295 ± 51 nm for CNFs carbonized at 600, 800, and 1000 °C, respectively. Subsequently, a clear trend in diameter change depending on the carbonization temperature between 600 and 1000 °C is not observed, which is in agreement with the literature.[7]

2.2. Microscale Electrical Properties

At the microscale, electrical properties have been analyzed by PF TUNA contact current maps. The contact current maps were simultaneously recorded with the topography maps and are shown in **Figure 2**. The topography maps, shown in Figure 2a–e, exhibit randomly oriented and well interconnected CNFs with similar morphologies independent of the exact carbonization temperature. In contrast to the overall similar morphologies, the simultaneously captured corresponding current maps, shown in Figure 2f–j, differ significantly as a function of the carbonization temperature. Although CNFs carbonized at 600 °C (Figure 2f) were analyzed with an elevated bias voltage of 100 mV, only low currents in the order of a few pA were observed. The current maps, depicted in Figure 2g–j, were acquired at a bias voltage of 20 mV and exhibit currents up to tens of nA for the CNFs carbonized at 900 and 1000 °C.

The voltage source was located about 100 ± 10 µm from the AFM tip. Therefore, to record a current signal, an electron percolation path from the voltage source through multiple CNFs and thus, CNF interconnections needs to be present. According to the current maps displayed in Figure 2f–j, and the visible substantial currents along CNFs, percolation paths exist in every analyzed CNF. This observation underlines the good interconnections of CNFs within the networks, as already observed morphologically in Figure 2a–e. However, it is important to carefully analyze the current maps, as a larger tip-surface contact area is prone to result in larger current values at these positions. This effect is observed at the edges of single fibers (Figure 2f,h and partially 2i) where the side of the tip rather than the foremost tip apex is in contact with the CNFs. To eliminate these edge effects and enable an exact quantitative analysis of currents, high-resolution 200 nm × 200 nm current maps were acquired on different individual CNFs within the fiber network for each sample.

2.3. Nanoscale Electrical Properties

Figure 3 shows an examplary series of AFM images with a sequentially increased magnification for CNFs carbonized at 700 °C. The dashed boxes in Figure 3a–d indicates the zoom area for each subsequent magnified scan. Thereby, the exact position of the measured area on the CNF network is known. Comparison of Figure 3a and its subsequent zoom, shown in Figure 3b, shows that the fiber morphology can be displayed reproducibly emphasizing the non-destructive AFM character and the measurement's stability. Figure 3c shows a fiber intersection with

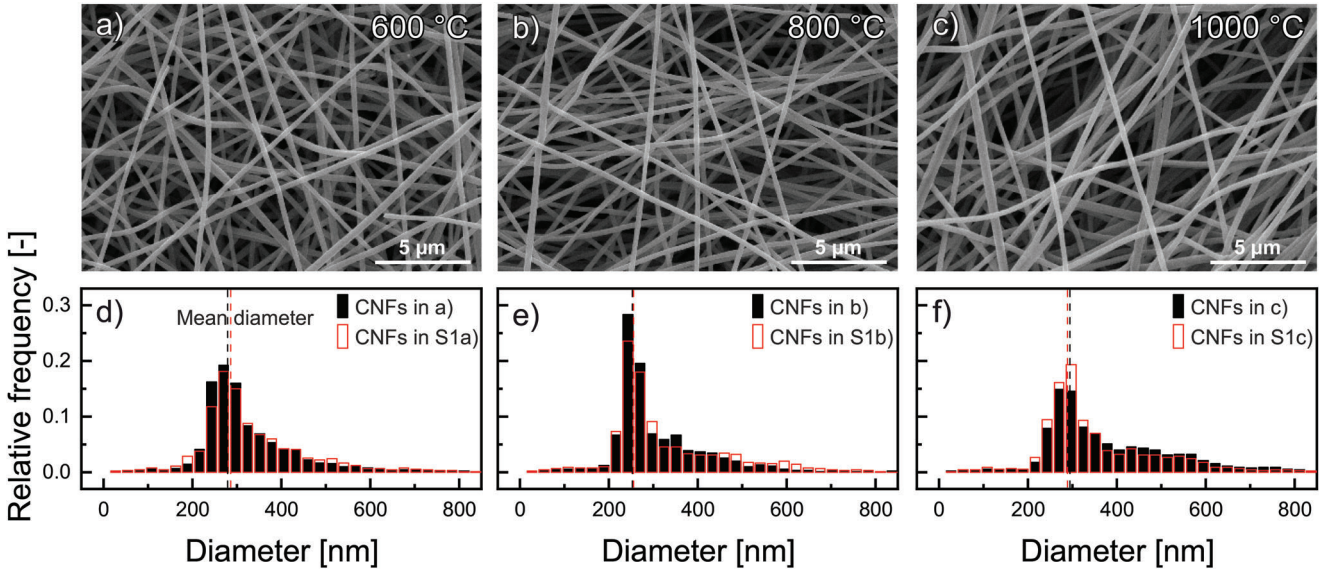

Figure 1. a–c) SEM images of CNF mats carbonized at temperatures of 600 °C (a), 800 °C (b), and 1000 °C (c) are shown. The CNFs are mostly straight with no preferred orientation and exhibit similar diameters. d–f) Histograms exhibiting the respective relative diameter frequencies determined by the DiameterJ algorithm.[47] Analyzing an SEM image from another spot for each sample, displayed in Figure S1a–c (Supporting Information), yields a comparable diameter distribution (red bars). The dashed lines indicate the averaged diameters.

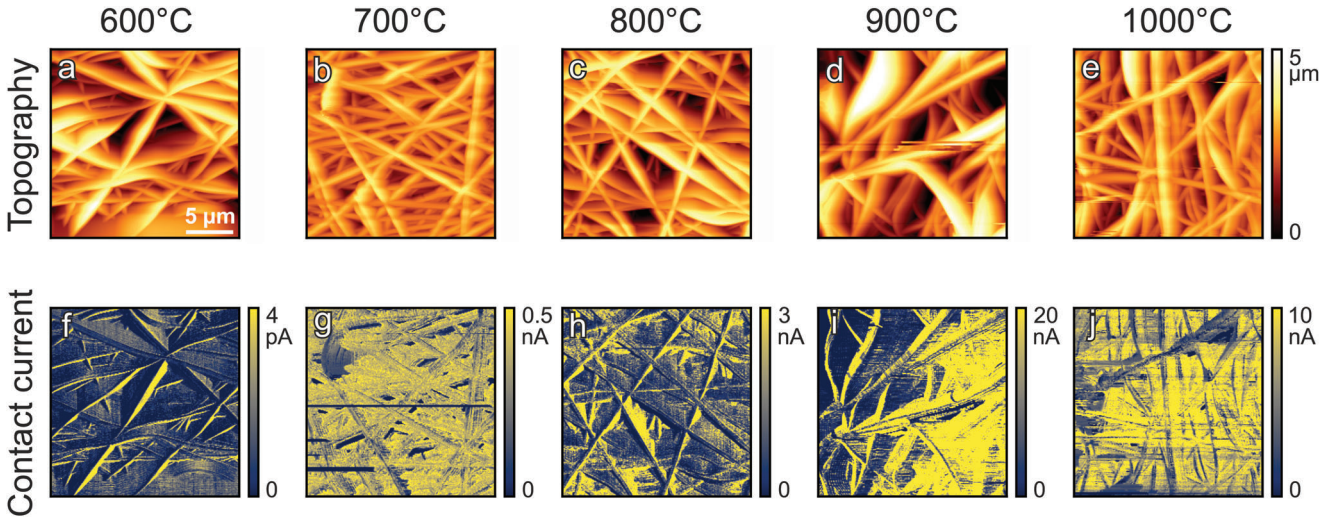

Figure 2. a–e) 20µm × 20µm topography maps showing the CNF mats carbonized at temperatures ranging from 600 to 1000 °C. All samples exhibit a fibrous morphology with randomly oriented CNFs. f–j) Respective simultaneously acquired contact current maps showing that currents were sensed with a broad spatial distribution and along all CNFs. The CNFs carbonized at temperatures between 700 and 1000 °C (g–j) were measured with a bias voltage of 20 mV, while the CNFs carbonized at 600 °C (f) were measured with a bias voltage of 100 mV to overcome the current detection limits.

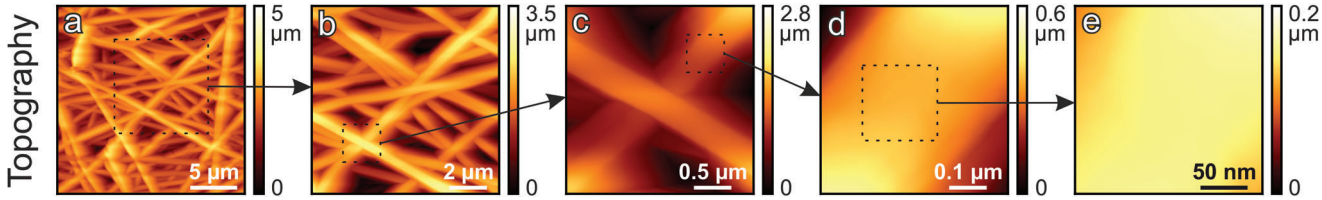

Figure 3. a–e) Topography maps showing an examplary series of AFM images with a sequentially increased magnification for CNFs carbonized at 700 °C. The dashed boxes in the larger topography maps in (a–d) indicate the location of each subsequent map. Finally, the high-resolution 200 nm × 200 nm map in (e) exhibits the uppermost exposed part of an individual CNF.

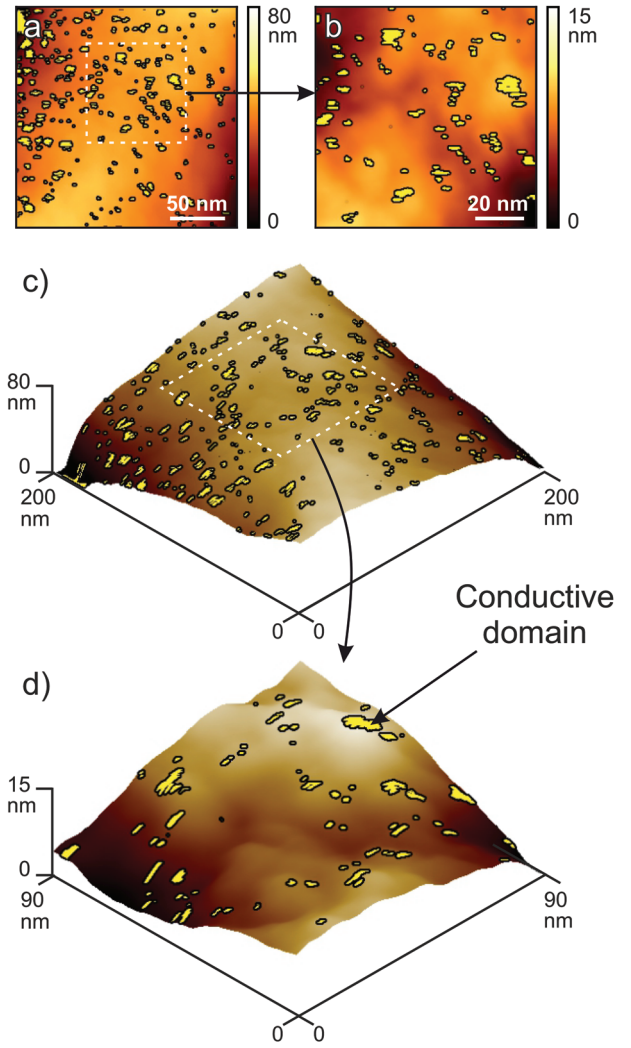

Figure 4. a) High-resolution 200 nm × 200 nm topography map of a typical CNF, carbonized at 800 °C. The yellow spots originate from the simultaneously acquired current maps and indicate conductive surface domains on which currents above 10 pA were observed. The dashed box indicates the zoom for the subsequent map in (b). c,d) Additionally, both maps are displayed in 3D to accentuate the CNFs curvature (c) and the conductive surface domain distribution on the particle-like CNF structure (d).

two CNFs overlapping each other. Finally, Figure 3d shows a single fiber with visible curvature. The highest resolution scan in Figure 3e shows the uppermost exposed part of the fiber, thus, ensuring that only the foremost tip apex is in contact with the fiber, which is a necessity for the precise analysis of the nano-electrical properties without edge effects.

Figure 4a shows a 200 nm × 200 nm topography map of a typical CNF carbonized at 800 °C. The yellow overlayed spots originate from the simultaneously acquired contact current map and indicate the conductive surface domains where currents above 10 pA were observed. The conductive surface domains are a few nanometers in size and are randomly distributed among the exposed CNF surface. The dashed box in Figure 4a indicates the zoom area which is displayed in Figure 4b. Additionally, the same maps are illustrated in 3D, which is shown in Figure 4c,d. Figure 4c accentuates the curvature of the individual fiber, while Figure 4d highlights the nanoscale structure. Particle-like structures of tens of nanometers are visible, which is in agreement with transmission electron microscopy (TEM) images acquired during in situ carbonizations under vacuum.[22] Conductive surface domains are found on top of such particle-like structures as well as on their sides and in valleys. Current maps acquired on another CNF carbonized at 800 °C (Figure S2, Supporting Information) underline the presence of such randomly distributed conductive and highly resistive surface domains on the CNFs' surfaces.

The finding, that a large fraction of the CNFs' surface area is highly resistive, is striking. The observation of a significant ratio of highly resistive areas on individual CNFs, and thus, representation of a strong limitation of the overall CNFs' conductivity, is attributed to two effects: First, highly resistive surface areas indicate the presence of highly resistive surface species, due to disordered carbon structures. Their presence is in agreement with earlier reported STM observations,[30] and TEM images.[22,48] Furthermore, surface oxides, which were reported in an X-ray photoelectron spectroscopy (XPS) study,[12] increase the resistivity of carbons.[49] Second, highly resistive surface domains indicate the absence of electron percolation paths in the bulk volume, although the CNF surface might be of ordered conductive crystalline structure. The reason for the absence of percolation paths can be highly resistive disordered turbostratic carbon structure in the bulk, which has a high porosity and low alignment.[50]

To analyze the effect of the carbonization temperature on the evolution of conductive surface domains, the 200 nm × 200 nm contact current maps of CNFs carbonized within the range of 600 to 1000 °C are compared. **Figure 5** shows the contact current maps, originating from two different fibers within the same sample for each carbonization temperature. All samples were measured at a bias voltage of 20 mV. Overall, the contact current maps depicted in Figure 5 clearly demonstrate the carbonization temperature dependence of the conductivity. The maximum measured currents and conductive area fraction rise with increasing carbonization temperature from 600 to 900 °C. The CNFs carbonized at 1000 °C exhibit similar maximum currents as the CNFs carbonized at 900 °C. Furthermore, an increase in the conductive area fraction is not clearly observable.

In the following, the 200 nm × 200 nm current maps of each sample are described individually. Figure 5a,b shows current maps of two fibers of the sample carbonized at 600 °C. Conductive surface domains are not identified. To the contrary, CNFs carbonized at 700 °C, visualized in Figure 5c,d, exhibits a few clearly conductive surface domains with maximum currents of around 0.1 nA and a few nanometers in size. Figure 5e,f displays the CNFs carbonized at 800 °C exhibiting even more conductive surface domains. The size of these conductive surface domains is comparable to those of the CNFs carbonized at 700 °C, but higher maximum currents of around 0.5 nA are observed. Both analyzed fibers are very homogeneous with respect to their conductive surface domain pattern and their measured currents. Figure 5g,h shows CNFs carbonized at 900 °C with conductive surface domains that are much larger than for CNFs carbonized at lower temperatures. While in Figure 5g a larger area fraction is conductive, Figure 5h shows less conductive area fraction. The maximum measured current values are similar for both

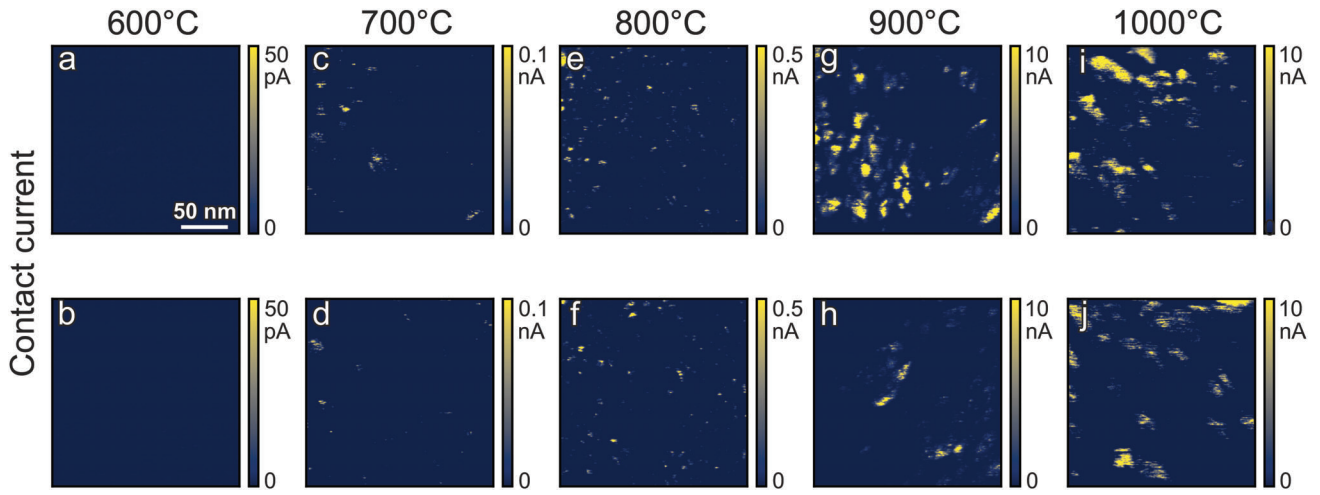

Figure 5. 200 nm × 200 nm high-resolution contact current maps of two different CNFs within a fiber network of each sample carbonized at temperatures within the range of 600–1000 °C. The current maps were acquired at a bias voltage of 20 mV simultaneously to topography maps such as seen in Figure 3e. The conductive area fraction and the maximum observed currents increase significantly with the carbonization temperature.

fibers with around 10 nA. Figure 5i,j shows CNFs carbonized at 1000 °C. Both CNFs exhibit, similarly to Figure 5g,h, larger conductive surface domains compared to the samples carbonized within the temperature range of 600–800 °C. The maximum measured currents are around 10 nA, and thus, comparable to the CNFs carbonized at 900 °C.

The increase in maximum measured currents and conductive surface domain size with raised carbonization temperature is attributed to the growth and better alignment of graphitic structures. This is in accordance with a selected-area electron diffraction (SAED) study,[23] where the authors report that the crystallites' in-plane-widths and vertical heights in CNFs increase from 1.4 to 2.0 nm and 1.0 to 1.2 nm, respectively, for an elevated carbonization temperature of 1000 °C compared to 600 °C. Similarly, a Raman study reported crystallite in-plane-widths of 1.5 nm to 2.47 nm for CNFs carbonized at 600 and 1000 °C, respectively.[27] The growth of conductive surface domains and their crystallites is promoted by the carbonization temperature dependent loss of heteroatoms, such as nitrogen, oxygen, and hydrogen,[7,12] that disturb the conductive carbon structure, and subsequent crosslinking, aligning, and merging mechanism of carbon structures.[23] The loss of heteroatoms results in an increase of bulk carbon content from 63.5 to 91.5% for a carbonization temperature increase from 600 to 1000 °C, as recently reported by elemental combustion analysis (CHNO).[12] In addition, while the authors reported a loss of oxygen in the CNF bulk detected by CHNO, the surface sensitive XPS characterization does not reveal any changes of the near-surface oxygen content with increasing the carbonization temperature from 600 to 1000 °C.[12] Therefore, variations in the conductive area fractions observed in Figure 5 are not associated with changing fractions of surface oxides, that were reported to influence the resistivity.[49]

To discuss the high-resolution 200 nm × 200 nm current maps of CNFs carbonized between 600 and 1000 °C, their histograms are analyzed as displayed in **Figure 6**a. The histograms exhibit the number of pixels, at which a current was detected, and their corresponding conductance. All histograms, illustrated in Figure 6a, show bell-shaped conductance distributions. Conductances of around 10^{-8} S are found for CNFs carbonized at 600 °C (bias voltage of 100 mV, cf. Figure S3, Supporting Information). The conductance distribution is comparably narrow and the histogram is cut-off at its left side due to detection limits at extremely low conductances. The CNFs carbonized at 700 °C show a symmetrically bell-shaped distribution exhibiting only few conductive spots on which conductances between 2×10^{-8} and 3.4×10^{-5} S are observed. Similarly, the CNFs carbonized at 800 °C also show a symmetrically bell-shaped conductance distribution, but with an increased number of conductive spots and a broader distribution ranging from 6.6×10^{-9} to 3.9×10^{-4} S.

While CNFs carbonized at temperatures within the range of 600–800 °C are represented by a single peaked distribution (Figure S4.1, Supporting Information), the conductance distributions of individual CNFs carbonized at 900 and 1000 °C are better represented by two peaks (Figure S4.2, Supporting Information). The individual peak locations are shown in Figure S5 and Table S1 (Supporting Information) for each carbonization temperature. CNFs carbonized at 900 and 1000 °C show conductances ranging from 2.2×10^{-9} to 7.6×10^{-3} S and 7.4×10^{-8} to 1.7×10^{-3} S, respectively. However, the description of the histograms at 900 and 1000 °C by two peaks indicates the occurrence of other carbon species. This might lead to a transition in electron transport mechanism from tunneling to direct transport, which is supported by the shift to a left-skewed bell shaped distribution for CNFs carbonized at 1000 °C. Furthermore, this is in agreement with XPS results exhibiting an increase of sp^2-hybridized carbons from around 65 % to 95 % of relative surface area for CNFs carbonized at 1000 °C compared to 900 °C.[7]

2.4. Correlating Macro- and Microscopic Electrical Properties

To understand the implications of the nano- and microelectrical findings for the macroscopic electrical performance, both macroscopic conductivities, determined by the four-point-method, and microscopic conductances, determined by analyzing the

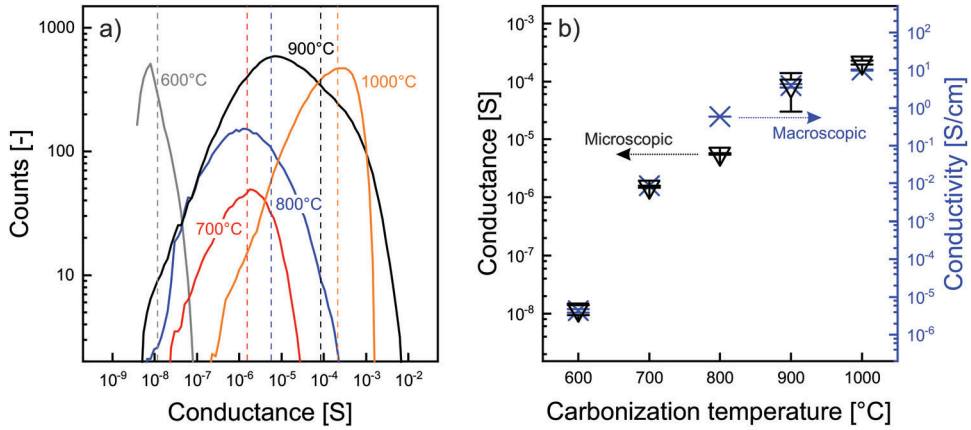

Figure 6. a) Conductance histograms, derived from analysis of the conductive area (currents above 1 pA) of the contact current maps shown in Figure 5c–j (bias voltage of 20 mV) and the contact current maps of the CNFs carbonized at 600 °C, shown in Figure S3e– f (Supporting Information) (bias voltage of 100 mV to overcome detection limits). The conductance was calculated by dividing the contact current by the bias voltage. The averaged conductance is not significantly influenced by changing the applied bias voltage, as shown in Figure S6 (Supporting Information). The histograms are plotted as average of two current maps for each sample and the histograms of individual CNFs are displayed in Figure S4.1–4.3 (Supporting Information). The dashed lines represent the averaged conductance of each sample. Furthermore, the averaged conductances of each sample are correlated with the macroscopic conductivities determined by the four-point-method, displayed in (b). The microscopic data exhibit a strong correlation with the macroscopic data and both depend on the carbonization temperature. Please note the logarithmic scales and the different units for conductivity and conductance.

nanoscale currents, are analyzed and correlated. Figure 6b shows the averaged conductances indicated already by the dashed lines in Figure 6a. The averaged conductance values range from 1.2 × 10^{-8} to 2.1 × 10^{-4} S for the 600 and 1000 °C CNFs, respectively. Macroscopic conductivity values on the same CNFs have been obtained by the four-point-method and range from 4.4 × 10^{-6} to 10.1 S cm^{-1} for the 600 and 1000 °C CNFs, respectively. These values are in accordance with published data.[7] Microscopic conductance by C-AFM and macroscopic conductivity from four-point-experiments are compared in Figure 6b, which clearly shows the strong correlation of electrical properties that are micro- and macroscopically determined by the carbonization temperature.

The strong correlation between microscopic and macroscopic results is striking, since macroscopic conductivity measurements were performed with electrodes at the mm scale, which are multiple orders of magnitude larger than the nanometer-scaled AFM tip. Similarly, both measurements contain contributions from the intrinsic CNF resistances and from the resistances between multiple CNF interconnections. In macroscopic experiments contact resistances are eliminated due to its four-point-setup. To the contrary, the microscopic conductances additionally contain these contributions from the contact resistances. Because of the comparably large contact area between voltage source and sample, this resistance can be neglected. The specific tip-sample contact resistance is assumed to be a rather constant factor for a given carbonization temperature, due to careful experimental conditions (slow scan rate, constant normal load). Furthermore, enlarging the distance between the voltage source (carbon tape) and area under investigation by the C-AFM experiment results in comparable recorded conductances (Figure S7, Supporting Information). This might indicate that the bulk CNF resistivity due to the interconnections of the fibers and the bulk fiber structure itself is not the overall limiting factor. Based on this work, either the absence of electron percolation toward the surface or the near-surface structure itself provides the limiting overall conductivities.

Figure 7a,b exhibits TEM images of fractured parts of the CNFs carbonized at 600 and 1000 °C. While both CNFs exhibit ordered and disordered structures, an increase in carbonization temperature clearly results in an increased order. The models, shown in Figure 7c–e, visualize the results of increasing conductive area fraction with raising carbonization temperature (cf. Figure 5). The structural models (Figure 7c–e) are schematically displayed as composition of highly ordered carbons (black and yellow) and less ordered carbons (grey), following Bennett's models derived from TEM images,[28,48] which is in agreement with near-surface TEM images of in situ carbonized CNFs reported in the literature.[22] The structure of a CNF carbonized at 600 °C, shown in Figure 7c, exhibits only few highly ordered carbon domains. Highly ordered carbon domains, which are highly resistive due to missing percolation paths (black) are present and only small high-resistance percolation paths to the surface exist (yellow). A large fraction of the carbon has a low order (gray). At carbonization temperatures of 800 °C, shown in Figure 7d, highly ordered carbon domains grow and thereby, previously highly resistive domains can form percolation paths and become conductive. At carbonization temperatures of 1000 °C, displayed in Figure 7e, the order increases and the fraction of highly ordered carbon domains is comparably large. However, the structure still exhibits highly resistive domains representing a strong limitation for an ideal macroscopic conductivity.

3. Conclusion

Carbonization temperature dependent micro- and nanoelectrical properties of electrospun PAN-derived CNFs have been investigated by means of PF TUNA, a C-AFM mode, to investigate

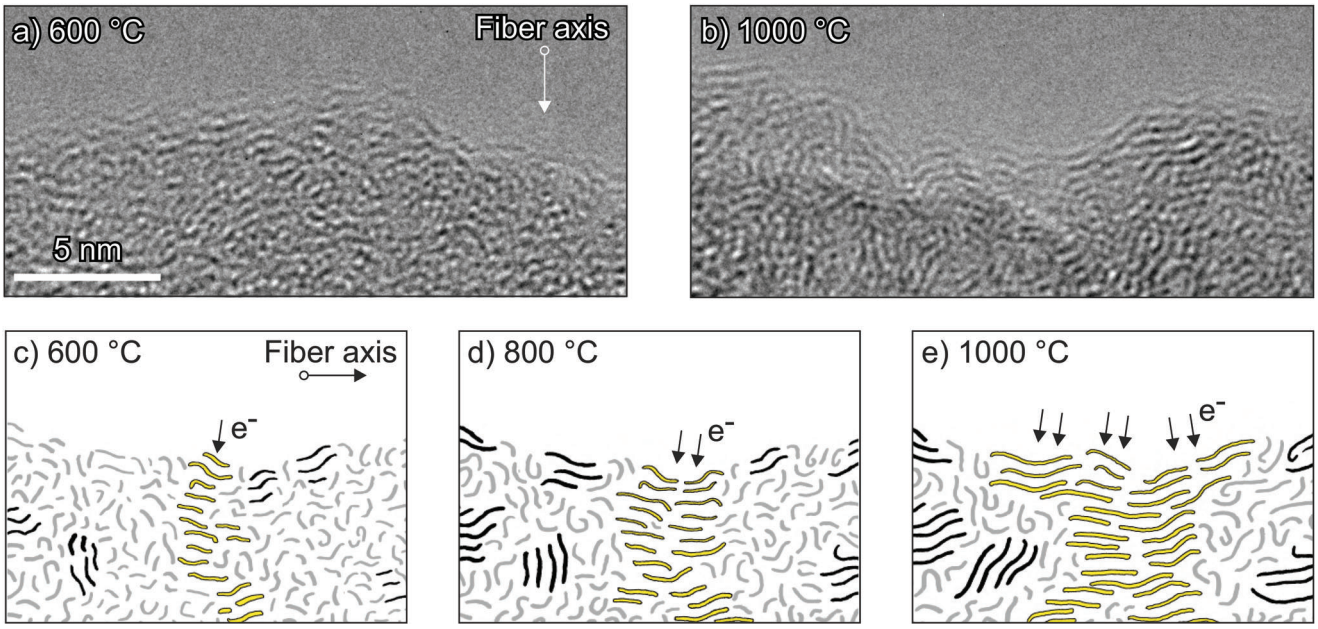

Figure 7. a,b) TEM images showing structures acquired at fractured parts of CNFs carbonized at 600 °C (a) and 1000 °C (b). Both exhibiting ordered and disordered domains, while the order increased with raising carbonization temperature. c–e) Models showing a schematic cross section of the near-surface structure for CNFs carbonized at 600 °C (c), 800 °C (d), and 1000 °C (e). The lines represent planes of highly ordered, potentially conductive, carbon structures (black and yellow) and less ordered, highly resistive, carbons (gray). However, current can only flow if highly ordered structures form electron percolation paths from the surface to the bulk (yellow). With increasing carbonization temperature the order of carbon structures increases, resulting in growing conductive surface and bulk structures, and thus, improved electron percolation.

factors limiting an ideal macroscopic conductivity. 20 µm × 20 µm contact current maps of CNF mats show electron percolation paths along all exposed CNFs with a homogeneous current distribution. For an exact quantitative analysis of nanoscale electrical properties, high-resolution 200 nm × 200 nm maps were recorded on individual CNFs within CNF mats carbonized at temperatures ranging from 600 to 1000 °C. In contrast to the homogeneous current distribution at the microscale, the nanoscale reveals heterogeneities within single CNFs. Remarkably, all CNFs still exhibit a large fraction of highly resistive surface domains on their nanoscale surface. This is attributed to either highly resistive carbon surface structures or the absence of electron percolation paths in the bulk volume. The conductive surface domains strongly depend on the carbonization temperature. For a bias voltage of 20 mV, no clearly conductive surface domains were found for CNFs carbonized at 600 °C, while on CNFs carbonized within the temperature range of 700–900 °C a stepwise increase in conductance and in the size of conductive surface domains is observed with increasing carbonization temperature. For CNFs carbonized at 1000 °C a further increase in the average conductance but no significant growth of the conductive surface domain size was observed. However, the histograms at 900 and 1000 °C indicate the transition from tunneling to direct electron-transport mechanism. The microscopic nanometer-scaled conductance measurements exhibit a strong correlation with the macroscopic conductivities recorded by the millimeter-scaled four-point-method, which are in agreement with literature. Based on the results in this study, either the absence of electron percolation paths toward the surface or the near-surface structure itself provides the limiting overall conductivities, rather than the bulk electron transport through multiple CNFs and their interconnections. However, a limitation of the AFM as described in the article is the undefined tip contact resistance. To overcome this, it is proposed to determine individual CNF's intrinsic and interconnection conductivities by microscopic four-point-measurements. Furthermore, correlating CNFs' crystallinities, for example, from spectroscopy or X-ray-based methods, with the results from this study, and investigating CNF cross sections might unravel the exact contribution of unformed percolation paths and disordered surface structures to the observed highly resistive surface. Such experiments would contribute to an even more complete picture of the nanoscale origins of the macroscopic electrical response of CNF networks.

4. Experimental Section

Synthesis of Carbon Nanofibers: All chemicals were used as received without further purification. A solution of 10 wt% polyacrylonitrile (PAN, homopolymer, 150 000 g mol^{-1}, BOC Science, USA) in *N,N*-dimethylformamide (DMF, VWR Chemicals, Germany) was obtained by dissolving 8 g of PAN in 72 g of DMF and stirring for two days at room temperature. PAN nanofibers were created by an electrospinning process using an electrospinning device equipped with a climate chamber (IME Technologies, The Netherlands). As a collector a rotating drum was used with a diameter of 6 cm and a rotation speed of 1500 rpm. The nozzle with an inner diameter of 0.8 mm was placed 15 cm away from the collector and moved parallel to the collector over a distance of 120 mm with a speed of 20 mm s^{-1} and a turn delay of 500 ms. The polymer solution was pumped through the nozzle with a flowrate of 40 µL min^{-1} and accelerated by a voltage of 25 kV. During the spinning process the climate was kept constant at 30% relative humidity and 25 °C. After 6 h of electrospinning the

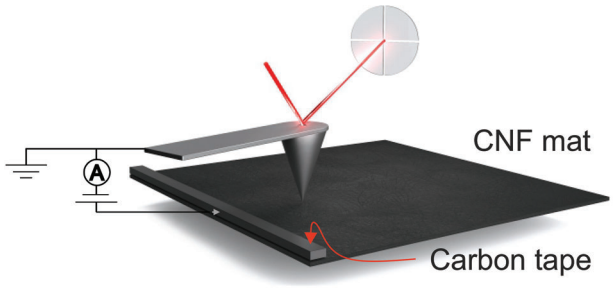

Figure 8. For the experimental setup, the 1 cm^2 CNF mats were electrically contacted with carbon tape from the top.

obtained PAN-nanofiber mat was removed from the drum collector and stabilized at 250 °C in air for 15 h in a drying furnace. Afterward, the fiber mat was carbonized in a tube furnace under argon atmosphere (5.2, Air Liquide) at various temperatures ranging from 600 to 1000 °C. The tube furnace was heated with a rate of 300 K h^{-1} to the desired temperature that was held for 3 h and then cooled with a rate of 200 K h^{-1}.

SEM Analysis: For the measurement of SEM images, a small part of the fiber mat (about 0.25–1 cm^2) was fixed to the sample holder with carbon tape. SEM images were acquired with a Quanta FEG 650 microscope (FEI, USA) equipped with an Everhart–Thornley detector. An acceleration voltage of 5 kV was used.

TEM Analysis: TEM images were recorded with Tecnai G2 F20 (FEI, USA) operated at 200 kV.[51] The CNF mats were dispersed in ethanol with an ultrasonic finger and one droplet was applied on a lacey carbon grid.

PeakForce Tunneling Atomic Force Microscopy: AFM measurements were performed with a Dimension Icon (Bruker, USA) in the current sensing and force-distance curve based PeakForce Tunneling Atomic Force Microscopy mode (PF TUNA, Bruker, USA). EFM tips (Nanoworld, Swiss) with a nominal spring constant of 2.8 N m^{-1} and an electrically conductive PtIr5 coating on the silicon tip have been employed and individually calibrated. The force–distance curve based mode was employed to avoid wear phenomena of the conductive coating. **Figure 8** illustrates the setup. A conductive carbon tape, mounted on the top of one side of the 1 cm^2 samples, ensured good electrical contact. All performed AFM scans were centered in a distance of around 100 µm from the carbon tape, if not stated differently. The bias voltage applied at the carbon tape was typically 20 mV or, if stated in the manuscript, 100 mV for CNFs carbonized at 600 °C. The high-resolution scans for quantitative analysis of electrical properties were measured with a constant maximum normal load of 6.5 nN and a slow scan rate of 0.5 Hz. If not stated differently, the scans consists of 256 × 256 pixels. As the bias voltage (Figure S3c–f, Supporting Information) and normal load (Figure S8, Supporting Information) influence the measured currents, both were chosen high enough to exceed currents above the detection limit (around 1 pA), but low enough to prevent high currents exceeding the saturation limit (1 µA). The recorded contact current was the current averaged over the tip–sample contact duration during each tapping cycle. 2D images were processed with pySPM package (v0.2.20) for Python.[52] 3D images were created with NanoScope Analysis software (v2.0, Bruker) and GIMP.

Measurement of the Electric Conductivity by the Four-Point-Method: The CNF mats were cut into rectangles with a side length of 3–6 cm. The thickness of the fiber mats was measured 5 times with a thickness dial gauge (Käfer Messuhrenfabrik, Germany), once in every corner and once in the center of the rectangular shaped mat. For the measurement of the conductivity, a Loresta GX with a LSP probe head (Nittoseiko Analytech, Japan) was used. The probe head featured a linear electrode assembly with four electrodes with an electrode-to-electrode distance of 5 mm. Each electrode pin has a rounded tip with a diameter of 2 mm. The probe head was placed in the middle of the sample parallel to the longer side of the CNF mat rectangle. The measured resistance was converted to a specific resistivity by the use of a resistivity correction factor (RCF) calculated by the device from the position of the probe head, and the dimensions of the CNF mat utilizing the Poissons equation as specified in the literature.[53]

Statistical Analysis: The statistical analysis of CNF diameters, shown in Figure 1d–f and Figure S1d–f (Supporting Information), was performed with DiameterJ (v1.018), which underlying algorithms are specified in the literature.[47] The analysis of two SEM images for each sample, segmented by DiameterJ's M1 thresholding, provided the respective diameter distribution. For each analyzed image, the relative frequencies were calculated by dividing the frequency counts for a specific diameter by the total frequency count.

The histograms shown in Figure 6a, derived from analysis of the current maps, shown in Figure 5c–j and Figure S3e–f (Supporting Information), and display the pixel counts and their respective conductances, considering only detected currents above the noise level (1pA). The classification was performed with 100 bins, with logarithmically equal size, between 10^{-10} and 10^{-2} S. The moving averages of five bins were determined and were displayed in all histograms.

Averaged values were presented as average value ± standard deviation.

Supporting Information

Supporting Information is available from the Wiley Online Library or from the author.

Acknowledgements

The authors thank L. G. J. de Haart for continuous support of this study. The funding for this work was provided by the Deutsche Forschungsgemeinschaft (DFG, German Research Foundation) under Germany's Excellence Strategy – Cluster of Excellence 2186 "The Fuel Science Center" – ID: 390919832. It also recieved funding from the Federal Ministry of Education and Research (BMBF) within Verbundvorhaben: Inkubator Nachhaltige Elektrochemische Wertschöpfungsketten (iNEW2.0) im Rahmen des Gesamtvorhabens Accelerator Nachhaltige Bereitstellung Elektrochemisch Erzeugter Kraft- und Wertstoffe mittels Power-to-X (ANABEL); FKZ 03SF0627A.

Open access funding enabled and organized by Projekt DEAL.

Conflict of Interest

The authors declare no conflict of interest

Data Availability Statement

The data that support the findings of this study are available from the corresponding author upon reasonable request.

Keywords

carbon nanofibers, electrical properties, microstructure

Received: January 31, 2023
Revised: April 20, 2023
Published online: April 27, 2023

[1] L. Zhang, M. Yin, X. Wei, J. Sun, D. Xu, *Anal. Biochem.* **2022**, *656*, 114882.
[2] W. Li, L.-S. Zhang, Q. Wang, Y. Yu, Z. Chen, C.-Y. Cao, W.-G. Song, *J. Mater. Chem.* **2012**, *22*, 15342.

[3] Z. Wang, S. Wu, J. Wang, A. Yu, G. Wei, *Nanomaterials* **2019**, *9*, 1045.
[4] K. Mondal, M. A. Ali, C. Singh, G. Sumana, B. D. Malhotra, A. Sharma, *Sens. Actuators, B* **2017**, *246*, 202.
[5] E. J. Ra, E. Raymundo-Piñero, Y. H. Lee, F. Béguin, *Carbon* **2009**, *47*, 2984.
[6] B. Kumar, M. Asadi, D. Pisasale, S. Sinha-Ray, B. A. Rosen, R. Haasch, J. Abiade, A. L. Yarin, A. Salehi-Khojin, *Nat. Commun.* **2013**, *4*, 2819.
[7] M. Gehring, H. Tempel, A. Merlen, R. Schierholz, R.-A. Eichel, H. Kungl, *RSC Adv.* **2019**, *9*, 27231.
[8] C. Xu, X. Li, T. Liu, H. Zhang, *RSC Adv.* **2017**, *7*, 45932.
[9] S. S. Manickam, U. Karra, L. Huang, N.-N. Bui, B. Li, J. R. McCutcheon, *Carbon* **2013**, *53*, 19.
[10] D. Yadav, F. Amini, A. Ehrmann, *Eur. Polym. J.* **2020**, *138*, 109963.
[11] M. Inagaki, Y. Yang, F. Kang, *Adv. Mater.* **2012**, *24*, 2547.
[12] A. Kretzschmar, V. Selmert, H. Weinrich, H. Kungl, H. Tempel, R.-A. Eichel, *ChemSusChem* **2020**, *13*, 3180.
[13] A. Kretzschmar, V. Selmert, H. Weinrich, H. Kungl, H. Tempel, R.-A. Eichel, *Chem. Eng. Technol.* **2021**, *44*, 1168.
[14] A. Kretzschmar, V. Selmert, H. Kungl, H. Tempel, R.-A. Eichel, *Microporous Mesoporous Mater.* **2022**, *343*, 112156.
[15] V. Selmert, A. Kretzschmar, H. Weinrich, H. Tempel, H. Kungl, R.-A. Eichel, *ChemSusChem* **2022**, *15*, 202200761.
[16] H. An, B. Feng, *Int. J. Greenhouse Gas Control* **2010**, *4*, 57.
[17] P. D. Sullivan, M. J. Rood, G. Grevillot, J. D. Wander, K. J. Hay, *Environ. Sci. Technol.* **2004**, *38*, 4865.
[18] L. Keller, T. Lohaus, L. Abduly, G. Hadler, M. Wessling, *Chem. Eng. J.* **2019**, *371*, 107.
[19] R. Shokrani Havigh, H. Mahmoudi Chenari, *Sci. Rep.* **2022**, *12*, 10704.
[20] Z. Zhou, C. Lai, L. Zhang, Y. Qian, H. Hou, D. H. Reneker, H. Fong, *Polymer* **2009**, *50*, 2999.
[21] F. Agend, N. Naderi, R. Fareghi-Alamdari, *J. Appl. Polym. Sci.* **2007**, *106*, 255.
[22] R. Schierholz, D. Kröger, H. Weinrich, M. Gehring, H. Tempel, H. Kungl, J. Mayer, R.-A. Eichel, *RSC Adv.* **2019**, *9*, 6267.
[23] J. Park, A. Kretzschmar, V. Selmert, O. Camara, H. Kungl, H. Tempel, S. Basak, R. A. Eichel, *ACS Appl. Mater. Interfaces* **2021**, *13*, 46665.
[24] E. Zussman, X. Chen, W. Ding, L. Calabri, D. A. Dikin, J. P. Quintana, R. S. Ruoff, *Carbon* **2005**, *43*, 2175.
[25] Y. A. Kim, T. Hayashi, M. Endo, M. S. Dresselhaus, in *Springer Handbook of Nanomaterials*, (Ed.: R. Vajtai) 1st Ed., Springer, Berlin, Germany **2013**, pp. 233–262, Ch. 7.
[26] D. Sebastián, I. Suelves, R. Moliner, M. J. Lázaro, *Carbon* **2010**, *48*, 4421.
[27] Y. Wang, S. Serrano, J. J. Santiago-Avilés, *Synth. Met.* **2003**, *138*, 423.
[28] S. Damodaran, P. Desai, A. S. Abhiraman, *J. Text. Inst.* **1990**, *81*, 384.
[29] P. J. Goodhew, A. J. Clarke, J. E. Bailey, *Mater. Sci. Eng.* **1975**, *17*, 3.
[30] W. P. Hoffman, W. C. Hurley, T. W. Owens, H. T. Phan, *J. Mater. Sci.* **1991**, *26*, 4545.
[31] K. Mondal, G. Pawar, M. McMurtrey, A. Sharma, *Mater. Today Chem.* **2020**, *16*, 100269.
[32] T. Maitra, S. Sharma, A. Srivastava, Y.-K. Cho, M. Madou, A. Sharma, *Carbon* **2012**, *50*, 1753.
[33] J. Cai, M. Naraghi, in *58th AIAA/ASCE/AHS/ASC Structures, Structural Dynamics, and Materials Conference*, American Institute of Aeronautics and Astronautics, Reston, VA, USA, ISBN: 978-1-62410-453-4, **2017**.
[34] A. F. Zapata-González, J. C. Cano-Franco, M. L. Álvarez-Láinez, *Adv. Mater. Lett.* **2019**, *10*, 539.
[35] D.-W. Kim, C. H. Kim, C.-M. Yang, S. Ahn, Y. H. Kim, S. K. Hong, K. S. Kim, J. Y. Hwang, G. B. Choi, Y. A. Kim, K. S. Yang, *Carbon* **2019**, *147*, 612.
[36] M. Panapoy, A. Dankeaw, B. Ksapabutr, *Thammasat Int. J. Sci. Technol.* **2008**, *13*, 11.
[37] Z. Zhang, W. Yang, L. Cheng, W. Cao, M. Sain, J. Tan, A. Wang, H. Jia, *ACS Sustainable Chem. Eng.* **2020**, *8*, 17629.
[38] S. Hasegawa, I. Shiraki, F. Tanabe, R. Hobara, T. Kanagawa, T. Tanikawa, I. Matsuda, C. L. Petersen, T. M. Hansen, P. Boggild, F. Grey, *Surf. Rev. Lett.* **2003**, *10*, 963.
[39] J. C. Li, Y. Wang, D. C. Ba, *Physics Procedia* **2012**, *32*, 347.
[40] P. G. Collins, M. Hersam, M. Arnold, R. Martel, P. Avouris, *Phys. Rev. Lett.* **2001**, *86*, 3128.
[41] C. S. Sharma, H. Katepalli, A. Sharma, M. Madou, *Carbon* **2011**, *49*, 1727.
[42] Y. Wang, S. Serrano, J. Santiago-Aviles, *J. Mater. Sci. Lett.* **2002**, *21*, 1055.
[43] H. Dai, E. W. Wong, C. M. Lieber, *Science* **1996**, *272*, 523.
[44] A. Trionfi, D. A. Scrymgeour, J. W. P. Hsu, M. J. Arlen, D. Tomlin, J. D. Jacobs, D. H. Wang, L.-S. Tan, R. A. Vaia, *J. Appl. Phys.* **2008**, *104*, 083708.
[45] W. Ali, V. Shabani, M. Linke, S. Sayin, B. Gebert, S. Altinpinar, M. Hildebrandt, J. S. Gutmann, T. Mayer-Gall, *RSC Adv.* **2019**, *9*, 4553.
[46] P. Butnoi, A. Pangon, R. Berger, H.-J. Butt, V. Intasanta, *J. Mater. Res. Technol.* **2021**, *12*, 2153.
[47] N. A. Hotaling, K. Bharti, H. Kriel, C. G. Simon Jr, *Biomaterials* **2015**, *61*, 327.
[48] S. C. Bennett, Ph.D. Thesis, University of Leeds, Leeds, UK **1976**.
[49] S. Barton, J. Koresh, *Carbon* **1984**, *22*, 481.
[50] S. Schimmelpfennig, B. Glaser, *J. Environ. Qual.* **2012**, *41*, 1001.
[51] M. Luysberg, M. Heggen, K. Tillmann, *J. Large-Scale Res. Facil.* **2016**, *2*, A77.
[52] O. Scholder, scholi/pyspm v0.2.20, **2019**, https://doi.org/10.5281/zenodo.2650457, (accessed: January **2023**).
[53] M. Yamashita, M. Agu, *Jpn. J. Appl. Phys.* **1984**, *23*, 1499.